Journal of Electroanalytical Chemistry 897 (2021) 115556

Contents lists available at ScienceDirect

Journal of Electroanalytical Chemistry

journal homepage: www.elsevier.com/locate/jelechem

The roles of constituting oxides in rare-earth cobaltite-based perovskites on their pseudocapacitive behavior

Miroslav M. Pavlović [a,b,*], Marijana R. Pantović Pavlović [a,b], Sanja G. Eraković Pantović [a], Jasmina S. Stevanović [a,b], Srećko R. Stopić [c], Bernd Friedrich [c], Vladimir V. Panić [a,b,d]

[a] Institute of Chemistry, Technology and Metallurgy, National Institute of the Republic of Serbia, Department of Electrochemistry, University of Belgrade, Belgrade, Serbia
[b] Center of Excellence in Environmental Chemistry and Engineering - ICTM, University of Belgrade, Belgrade, Serbia
[c] Process Metallurgy and Metal Recycling, RWTH Aachen University, Aachen, Germany
[d] State University of Novi Pazar, Department of Chemical-Technological Sciences, Novi Pazar, Serbia

ARTICLE INFO

Keywords:
Capacitive interactivity
Strontium oxide in mixed capacitive materials
Capacitor electrodes
Oxide composites

ABSTRACT

The role and influence of strontium and its oxide on structure and capacitive response of materials containing mixed lanthanum cobalt oxides, LC, and lanthanum strontium cobalt oxides, LSC, as a capacitive materials were investigated in this study. The mixed oxides were synthesized by the single-step ultrasonic spray pyrolysis (USP) technique. The microstructures and electrochemical properties of the samples were characterized by X-ray diffraction, scanning electron microscopy, cyclic voltammetry, potentiostatic electrochemical impedance spectroscopy and galvanostatic charge/discharge cycling. It was found that strontium oxide induces the formation of the perovskite structure of promoted pseudocapacitive behavior over an enhancement of redox transitions of cobalt. The measurements showed that the capacitive stability and rate capability were lower for the samples of higher specific capacitance. Among the prepared materials, the LSC prepared at a USP temperature 600 °C showed the best capacitive characteristics in 0.10 M KOH due to having the most defined spherical perovskite structure leading to well-defined reversible charge–discharge performances.

1. Introduction

In order to reach highly reversible and stable materials for energy storage processes, investigation of novel materials, as suitable supports for noble ones, has been predominant in the past few years [1-9].

Perovskite oxides are promising candidates for electrochemical power sources due to their unique physical and electronic properties, of which its structural stability is one of the most important. Perovskites can accommodate mobile oxygen ions under electrical polarization. It was shown that oxygen ion mobility and vacancies play an important role in charge storage and in catalysis in general [10]. The composition and structural stability of Perovskite not only allow storage of large quantities of energy, but also ensure high rates of delivery [11].

Alkaline-stable perovskite materials with the general formula ABO_3 (where A is a lanthanide and B is a transition metal) were proven to have metallic conductivity and some redox capacitive behavior [10-17], which makes them promising candidates as supports in supercapacitive materials support of reversible and stable response. Oxygen-vacancy-mediated redox pseudocapacitance for a nanostructured lanthanum-based perovskite, $LaMnO_3$ was demonstrated for the first time for fast energy storage [10]. Rare-earths in ruthenates are also known for improvement of the specific capacitance, especially La replacement in $SrRuO_3$ [12]. ABO_3 materials with high electrochemical stability and fast charge/discharge rates can be synthesized in different material combinations [6,7,15,18-20]. It was found recently that simple impregnation of $LaSrCoO_3$ with RuO_2 leads to considerable mutual enhancement of the capacitive behavior of these two structural components [6]. Similarly, the synergy of Co/Mo has good redox ability and it facilitates high oxygen mobility, fast kinetics of charge storage and excellent cycle life [21].

As a synthesis procedure, a unique ultrasonic spray pyrolysis. (USP), was applied that appeared to be a highly promising technique for the synthesis of perovskite materials [6,22]. It was found that certain USP-synthesized perovskites as solid electrolytes have the ability to improve the performance of solid oxide fuel cells (SOFC) [22].

Perovskite materials can have long cyclability compared to carbon-supported composites in alkaline to neutral media [3,23]. Lanthanum

* Corresponding author at: Institute of Chemistry, Technology and Metallurgy, National Institute of the Republic of Serbia, Department of Electrochemistry, University of Belgrade, Belgrade, Serbia.
E-mail address: mpavlovic@tmf.bg.ac.rs (M.M. Pavlović).

https://doi.org/10.1016/j.jelechem.2021.115556
Received 19 April 2021; Received in revised form 19 July 2021; Accepted 20 July 2021
Available online 25 July 2021

cobaltites (LC) and strontium-impregnated lanthanum cobaltites ($La_{1-x}Sr_xCoO_{3-\delta}$, LSC) are supposed to have wider voltage window than carbonaceous materials [4,6].

Although the perovskites have been proven to be of pronounced capacitance with respect to the constituting oxides, the roles and influences of the separate components in the capacitive responses of enhancing perovskite structures are not clear. Zhang et al. [23] performed ex situ doping of LC with Sr oxide and found some improvements in the electrode capacitive response and also nickel foam supported asymmetric capacitor. However, the unique redox influence of strontium oxide doping into the structure of LC was not reported.

The aim of the reported investigation was to bring detailed insights concerning separated influences of constituting oxides to this issue, in order to reveal the redox electrochemistry behind perovskite structures as supports for supercapacitive applications. The synthesis approach involved in situ impregnation of the LC structure with Sr oxide.

LC, as the "Sr-free" counterpart of strontium-doped lanthanum cobaltite (LSC) nanopowders were also synthesized by the ultrasonic spray pyrolysis process and their structural and capacitive properties were analyzed and compared.

2. Experimental

2.1. Synthesis of $LaCoO_3$ and $La_{0.6}Sr_{0.4}CoO_3$ powders by ultrasonic spray pyrolysis

The synthesis of Co-based perovskites was realized by single-step USP procedures. The solutions for the syntheses of LC and LSC were prepared by mixing solutions of the starting precursors in stoichiometric mole ratios, i.e. La:Co = 1:1 for LC and La:Sr:Co = 3:2:5 for LSC. An La:Sr ratio of 3:2 was chosen in order to prepare stoichiometric $La_{0.6}Sr_{0.4}CoO_3$ perovskite, according to a previously published work [6]. Aqueous 0.10 M solutions of $La(NO_3)_3{\cdot}6H_2O$ (99.9% rare earth oxide), $Sr(NO_3)_2$ (99 %) and $Co(NO_3)_2$ (98%), all from Alfa Aeser, were used as precursors for the synthesis of LC and LSC. The USP conversion temperature was adjusted and controlled using a thermostated furnace. All powders were synthesized by ultrasonic spray pyrolysis in equipment with horizontal nebula flow.

Fogging of the prepared precursors solutions occurred in an ultrasonic atomizer (Gapusol 9001, RBI/France) with an ultrasonic nebulizer (Prizma Kragujevac, Serbia) to create an aerosol [6,24]. The aerosol with droplets having diameter of around 2.3 μm was produced with an ultrasound frequency of 2.5 MHz [6,25]. The atomization was performed in an O_2/N_2 atmosphere as carrier gas, having O_2 to N_2 volume ratio of 2:1 and continuous flow rate of 3 $dm^3\ min^{-1}$. The synthesis temperature was adjusted to 600 °C or 800 °C for both LC and LSC, in order to investigate the influence of these USP synthesis conditions. The produced LC and LSC particles were collected in water bottle collectors.

3. Characterization techniques

3.1. Surface morphology and structural analysis

The morphology and elemental composition of LC and LSC powders were analyzed by scanning electron microscopy (SEM) and energy dispersive X-ray spectroscopy (EDS). Scanning electron microscopes (Zeiss DSM 982 Gemini; Vega TS 5130 MM Tescan) were used to examine the appearance of the obtained particles. The elemental composition was determined by EDS with a Si(Bi) X-ray detector connected to the SEM and a multi-channel analyzer. The identification of elements was performed via the unique set of peaks from the reflected X-ray spectrum.

Structural and phase analysis of the composite samples were examined by X-ray diffraction (XRD) measurements on a Philips PW 1050 (Royal Philips, Amsterdam, the Netherlands) powder diffractometer at room temperature with Ni-filtered CuKα radiation (λ = 1.54178 Å) and scintillation detector within the 2θ range of 10–82° in steps of 0.05°, at a scanning rate of 5 s per step. Phase analysis was performed using EVA v. 9.0 software.

3.2. Electrochemical measurements

Electrochemical properties of LC and LSC were studied by cyclic voltammetry (CV), potentiostatic electrochemical impedance spectroscopy (PEIS) and galvanostatic charge–discharge (GCD) tests. The electrochemical measurements were performed in a conventional three-electrode cell. A platinum wire and Ag|AgCl were used as counter and reference electrode, respectively. All potentials in the discussion are referred to Ag|AgCl. The working electrode was glassy carbon (GC, Sigradur – Sigri, Elektrographite, GmbH, Germany) with a surface area of 0.196 cm^2 covered by a thin layer of LC or LSC according to the following procedure: 20 μL of LC or LSC water suspension (5 mg mL^{-1}) was added onto the GC using a micropipette. The mass loading of both LC and LSC electrode materials was 0.51 mg cm^{-2}. After 2 h of drying in air, the same volume of nafion solution (1:100 vs. water), achieved by dissolving 10 μL of nafion perfluorinated resin solution in 990 μL of water, was added on top of the layer and left to additionally dry at room temperature. This very thin nafion film was used for binding the investigated powders to the GC substrate. The cell was purged with N_2 for 30 min prior to CV electrochemical measurements. A potentiostat/galvanostat measuring station (BioLogic SAS, SP-240, Grenoble, France) provided with physical electrochemistry software was used. The CV responses in 0.10 M KOH were recorded at a scan rate of 50 mV s^{-1}. The specific capacitance, the most important indicator for the evaluation of electrode properties for supercapacitors [7,22,23], was calculated from the CV data according to Eq. (1):

$$C_{sp} = \frac{1}{m\upsilon(\Delta E)} \int_{Ea}^{Ec} I(E)dE \quad (1)$$

where C_{sp} (F g^{-1}) is the specific capacitance, m (g) is the mass of the active material, $\int_{Ea}^{Ec} I(E)dE$ (A V) is the integral area under the CV curve, which gives the charge stored during cathodic and anodic scans, υ (V s^{-1}) is the scan rate, and E_a and E_c (V) are the anodic and cathodic integration limits of the potential or the capacitive potential window.

PEIS studies were performed in the frequency range of 10^{-2}–10^6 Hz using a 10 mV root mean square sinusoidal potential amplitude around the potentials 0.1 and 0.3 V for all the samples. These potentials are recognized as characteristic values according to the CV responses. The impedance spectra were analyzed and fitted by ZView® software [28-30].

GCD tests were performed for cycle-life assessments of all the samples. These tests were also performed on potentiostat/galvanostat station (BioLogic SAS, SP-240, Grenoble, France). Galvanostatic charging and discharging curves were measured at a 50 μA current density until the 600 mV voltage window is spent (adopted from the CV measurements). The specific capacitances were calculated by graphical differentiation according to the following equation [18,31]:

$$C_{sp} = \frac{Idt}{mdE} \quad (2)$$

where C_{sp} (F g^{-1}) is the specific capacitance, I (A) represent the charge/discharge current, dt (s) is the time required to spend the infinitesimal potential window, dE (V), and m (g) represents the mass of the active material.

4. Results and discussion

4.1. SEM and EDS analysis

The porosity of a material governs the maximal availability of the active sites [6,25,26]. The morphologies of the LC and LSC powders produced at 600 and 800 °C are presented in Fig. 1, which shows the typical appearance of the produced materials under SEM examination. The EDS elemental compositions of produced powders is presented in Table 1.

The lanthanum cobalt oxides powder synthesized at 600 °C (LC 600, Fig. 1a) is highly agglomerated and aggregated. The tight agglomerates consist of almost spherical particles in the size range of 50 nm – 200 nm. The temperature of the synthesis plays an important role. The influence of temperature could be seen by comparing powders from Fig. 1a and Fig. 1b. The later shows the appearance of lanthanum cobalt oxides powder synthesized at 800 °C (LC 800). The particles appear considerably less agglomerated, and the formed spherulites are in the size range of 1 μm. The initial particle sizes are also in the range of 50 nm – 200 nm, but the aggregation is not as pronounced as for the LC 600. The above mentioned features are more clearly seen in Fig. 2, which shows LC 600 and LC 800 at higher magnification. While the aggregated matrix LC 600 is formed of uniformly-sized elemental particles, the more porous structure of LC 800 appears to gather these particles into nonuniformly-shaped agglomerates tending to form huge spheroidal shapes. It follows that the lower USP temperature is not sufficient to convert the fine droplet structure of the aerosol into the spherical structure of the synthesized powder.

The LSC powder synthesized at 600 °C (LSC 600) is shown in Fig. 1c. Comparing to Fig. 1a and Fig. 1b, the influence of Sr is evident. The powder is more spherical, more rounded and more compact, with clearly defined pores between the uneven spheres, which is in correlation with the results of previous research [6]. The sphere size of the powder is in the range of 1 μm − 2 μm, with the majority of particles having a diameter of 1 μm. The $La_{0.6}Sr_{0.4}CoO_3$ powder synthesized at 800 °C (LSC 800) is shown in Fig. 1d. The influence of synthesis temperature on the powder morphology is evident once again, along with the fine sphere-generating influence of strontium oxide. The powder particles are well defined fluffy spheres with the powder sphere size in the range of 0.5 μm – 1.5 μm. It could be noticed from Fig. 1 that both the synthesis temperature and presence of strontium ions influence the morphology of the powder in the sense that spherical particles become well defined, more rounded and larger. The unique finding is that strontium forms fluffy structure at the surface of the spherical particles at higher temperatures. This could indicate that some structural composition occurs upon insertion of strontium oxide at higher temperatures.

EDS composition mapping was performed on the powder particles at different spots and different samples and the average value of these elemental compositions are listed in Table 1.

As it could be seen in Table 1, the detected content ratios of Co to La for LC powders are considerably higher with respect to stoichiometric 1:1. As the material becomes less compact and more porous at higher temperature (Figs. 1 and 2), the ratio indicates slightly higher presence of La. This enrichment in Co also holds for the LSC sample. However, the contents of La and Sr are lower at higher temperature, which also generates the fluffy surface structure of the spheres. It appears that the Co oxide tends to grow into surface needles, which mask the EDS response of the La and Sr oxides. The stoichiometric ratio of La to Sr of 3:2 appears well preserved in the LSC samples. It could be hypothesized that besides perovskite LC and LSC powders, some separate phases of Co-based oxides are formed. This hypothesis was further investigated by XRD measurements.

4.2. X-ray diffraction analysis

The XRD patterns of LC 600, LC 800, LSC 600 and LSC 800 powders are presented in Fig. 3. Sharp peaks appear in the 2θ range of 10–80° for all the samples. These XRD peaks could be assigned to LC and LSC compounds with the sharpness indicating the highly crystalline sin-

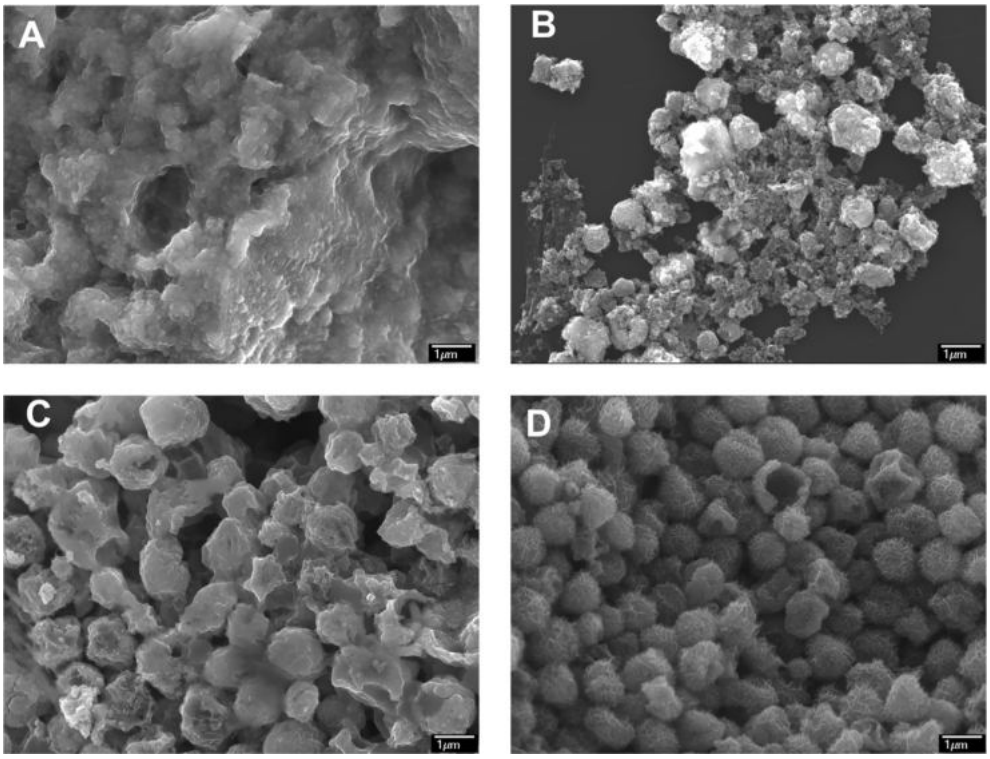

Fig. 1. Typical SEM microphotographs of LC powders synthesized at: a) 600 °C and b) 800 °C, and LSC powders synthesized at c) 600 °C and d) 800 °C.

Table 1
EDS comparative analysis of LC 600, LC 800, LSC 600 and LSC 800 as-prepared powders (at.%).

Element/ at. %	LC 600	LC 800	LSC 600	LSC 800
O	61.8	69.0	64.1	64.2
Sr	–	–	4.2	2.8
La	1.9	2.3	6.5	4.5
Co	36.3	28.7	25.2	28.5

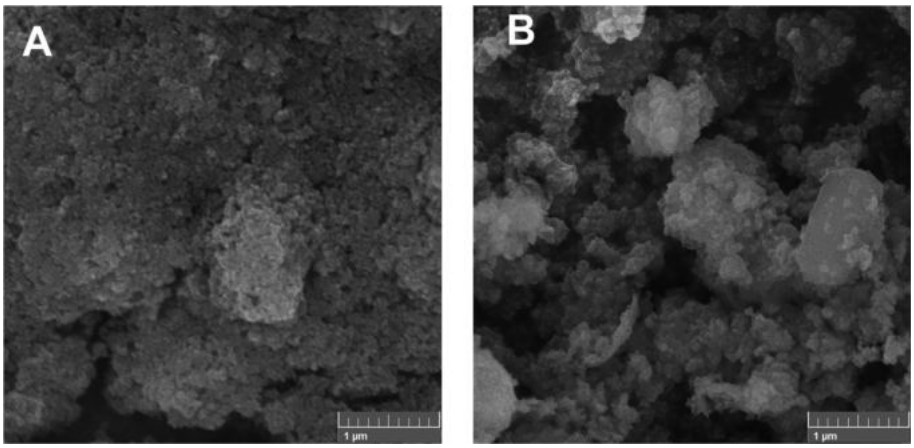

Fig. 2. SEM microphotographs of lanthanum cobalt oxides powders synthesized at: a) 600 °C and b) 800 °C recorded at magnification of 50 k.

gle–phase nature of the samples with a rhombohedral crystal structure. The synthesized LC and LSC powders as perovskites, with variation in the crystal structure that can lead to distinct electrocatalytic activities [6,27]. The diffraction peaks of Co_3O_4 (JCPDS PDF No.01–078-1969), La_2O_3 (JCPDS PDF No.01–074-2430), CoO (JCPDS PDF No.01–089-2803) and SrO (JCPDS PDF No.00–048-1477) could be distinguished in the XRD patterns of LC and LSC. It can be derived from these XRD findings that there is formation of nanoparticles of above mentioned compounds.

Besides the good correlation to the development of perovskite structure (mixed oxide) for all the samples it could be seen that there is some significant quantity of a separate Co_3O_4 crystal phase in the LC 600, LC 800 and LSC 600 samples, and to very small extent of CoO phase in the LSC 800 sample. This confirms that the generation of separate Co oxide phase, beside that incorporated into perovskite structure, could aggregate separately within the powder particles, as indicated by the EDS measurements.

Apart from separate phases of Co oxides, the XRD patterns also indicated the appearance of separate La_2O_3 (for LC) and SrO (for LSC) phases. The peaks of La_2O_3 are more pronounced in the high temperature sample, which agrees with higher La/Co ratio found by EDS.

4.3. Electrochemical analysis and performances

Stable CVs of LC 600, LC 800, LSC 600 and LSC800 thin powder layers on GC substrate in 0.10 M KOH (nitrogen atmosphere) were recorded at the scan rate of 50 mVs^{-1}, and the results are shown in Fig. 4.

The cycling started from the open circuit potentials (OCP) for the prepared electrodes: −0.165 V for LC 600, −0.062 V for LC 800, 0.35 V for LSC 600 and 0.265 V for LSC 800. Although the OCPs were more positive when Sr was present, phenomenologically there is no great difference in the material response whether strontium was present or not. On the other hand, Sr influences development of the anodic branch in the materials synthesized at the lower temperature. Comparing the voltammograms of the obtained material to the ones for the Co_3O_4 in the same potential range of −0.1 V to 0.6 V in KOH electrolyte it could be concluded that some redox peaks appear

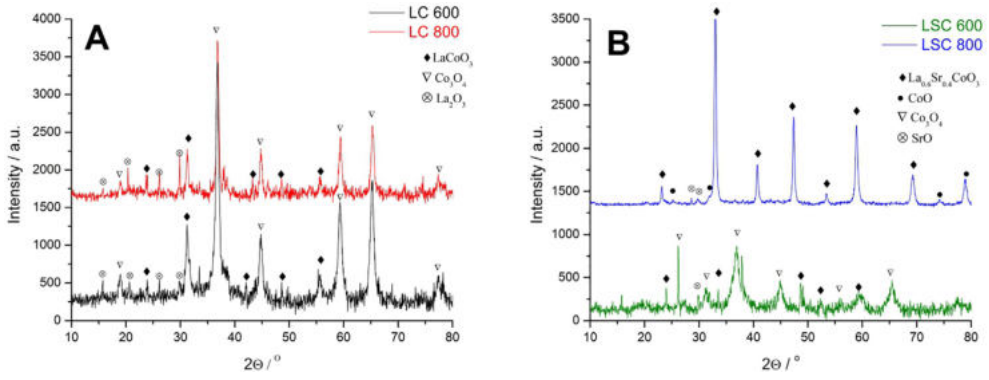

Fig. 3. XRD patterns of a) LC and b) LSC powders.

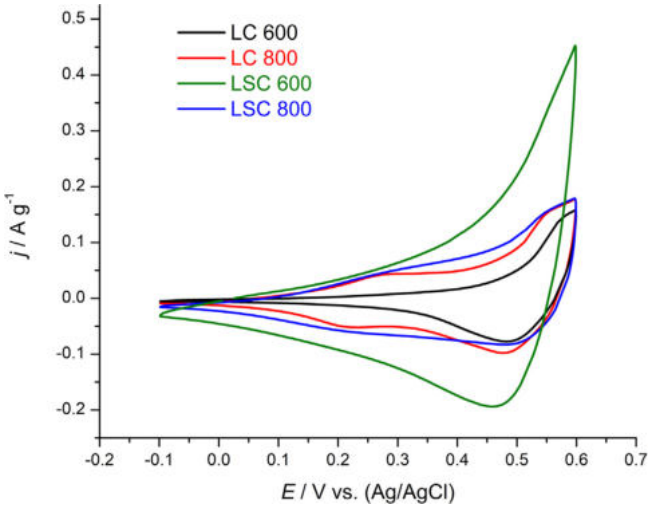

Fig. 4. Cyclic voltammograms of LC 600, LC 800, LSC 600 and LSC 800 at a scan rate of 50 mVs^{-1} in 0.10 M KOH in N_2 atmosphere at room temperature.

in the potential range of 0.4–0.6 V and are usually assigned to redox transitions of Co_3O_4 to CoOOH and CoOOH to CoO_2 [32]. The other weak broader peaks that appear outside this range could belong to the redox reactions of the rare earth metal. These curves are not close to the symmetric shape presented by an electrochemical double layer capacitor which has a closed rectangular shape and stores energy through non-Faradaic processes [32]. The voltammograms show forms that are typical of materials that are strongly governed by Faradaic processes with defined anodic and cathodic peaks that represent pseudocapacitive behavior. An effective symmetry might be associated with good reversibility of oxidation and reduction processes [33]. Poor linear behavior is affirmation of the pseudo-capacitive behavior of the electrode [34]. It was also shown that displacement of the oxidation peaks towards positive potentials and reduction peaks towards negative ones may be related to conductivity and to the polarization-induced capacitive ability of the electrode [35].

On comparing the LC and LSC CV curves, some differences could be noted. One of the major differences is the fact that the lowest CV currents are registered in the CV response of LC 600 and then in LC 800, which is an indication of the smallest active surface area of these electrode materials. Another difference reflects the fact that incorporation of Sr into the LC lattice leads to a considerable increase in the currents of recorded cyclic voltammetry at potentials greater than 0.0 V, which is not clearly evident at lower potentials. This promotes Sr, besides spherical shape and perovskite structure inducer, as the redox transition enhancing component in LSC. Both samples prepared at higher temperature (LC 800 and LSC 800) show a broad redox pair at around 250 mV. Although being quite weak, this shoulder-like anodic peak with cathodic counterpart could be distinguished for both samples prepared at 800 °C. On the other hand, a constant discharging current was registered in the potential region 400 down to 200 mV for LC 600 and down to 0.0 V for LSC 600 instead of the anodic peak that is present in the samples prepared at the higher temperature.

The C_{sp} of the samples was calculated by integrating the area delimited by the CV curve according to the Eq. (1). The following results for the specific capacitance were obtained: the lowest C_{sp} was 8.50F g^{-1} for LC 600, followed by 16.36F g^{-1} for LC 800, then 19.16F g^{-1} for LSC 800, and finally 34.94F g^{-1} for LSC 600. There are several conclusions that could be derived from the calculated and obtained results from the CV curves. Specific capacitance is lower for the samples not containing strontium, and this capacitance is up to 2–4 fold lower than for the Sr-containing samples. The temperature of the synthesis of an electrode material plays an important role. While for the samples not containing Sr, the higher temperature produces particles with higher specific surface area (Fig. 1), and hence having higher values of the specific capacitance, the inverse is applicable for the LSC samples. This could be associated to the Co oxide enrichment (opposite to LC, Table 1), which was found to cause the formation of the needles of the fluffy structure of the sphere surfaces. However, LSC 600 has higher specific capacitance compared to LSC 800, which does not present the benefits of needles formation. For better capacitive response of LSC, it seems that the not fully separated spheres of smooth surface (LSC 600, Fig. 1c) are beneficial. In addition, there is pronounced effect of multiple oxide structures present in the sample [6], especially separate Co_3O_4 phase (Fig. 3). Besides presence of separate cobalt oxide, the presence of strontium in perovskite structure leads to high electrode/electrolyte contact areas and high rates of electrode reaction [6], since an enhancement due to separate Co_3O_4 was not registered in the LC samples.

These findings are in good agreement with previously published results [6] for ruthenized LSC. They all confirm the statements that strontium influences the development of the anodic branch, and that the processing temperature plays an important role in electrode material production. It appears that not only Sr promotes the capacitive response of LC, but also LSC favors and enhances redox transition of material in higher oxidation states.

Potentiostatic electrochemical impedance spectroscopy (PEIS) tests were performed at potential of 100 (poor conductive region, Fig. 4) and 300 mV (fully developed redox transitions) to evaluate the details of capacitive response and electrochemical behavior for all of the samples, including hydrothermally prepared Co_3O_4 for the sake of comparison. PEIS of LC 600, LC 800, LSC 600 and LSC 800 thin powder layers on GC substrate were recorded in 0.10 M KOH at a perturbing potential of 10 mV in the frequency range between 10 mHz and 1 MHz and the results are shown in Fig. 5. Based on the PEIS data, Fig. 6 shows equivalent electrical circuit (EEC) models used to fit the data from Fig. 5 (EEC data are given by lines in Fig. 5).

The complex plane plots for LC and LSC all show two distinct regions. The first region consists of semicircle-like response at the high frequencies which corresponds to redox transitions and it reflects the charge transfer resistance-like (*R*3, Fig. 6) behavior of the electrode. The second region, represented by straight line in the low-frequency range, corresponds to -ionic exchange in the electrolyte/material interphase – external (CPE1) and internal (CPE2–CPE4)[36,37]. The high-frequency intersection of the curve with the real axis represents the resistance of the aqueous KOH solution (R1). The internal capacitive response (CPE2–CPE4) required series ionic (to CPE2 and CPE4) or material bulk (to CPE3) resistance represented by R2 in Fig. 6.

The results obtained for the examined materials from fitting results using EECs are given in Tables 2 and 3.

The constant phase element, CPE, is used in EEC instead of a capacitor, C, in order to better embrace the non-ideal behavior of the C element, namely to address the surface heterogeneities, surface roughness, as well as defects on the surface. In general, Eq. 3 is used as the definition of the impedance of the CPE:

$$Z_{CPE} = [Y(j\omega^{n}]^{-1}$$

where Y is the frequency-independent admittance of the CPE, ω being the angular frequency (ω = 2πf) in rad s^{-1}, f is the frequency, n is the value of the exponent of CPE between − 1 for an ideal inductor and 1 for an ideal capacitor.

The CPE1 element has the capacitive response that resembles the capacitive response of pure Co_3O_4. The C1 values of capacitance at 300 mV after fitting the results (Tables 2 and 3) are close to the value of pure Co_3O_4 (3.5 μF) which was fitted by simple RC EEC in series (Fig. 6c). This finding is in accordance with the XRD results of the prepared powders, which show the presence of separate Co_3O_4 phase besides the perovskite structure. The rest of the EEC circuit show interaction of Co_3O_4 with other oxide structures in the electrode material.

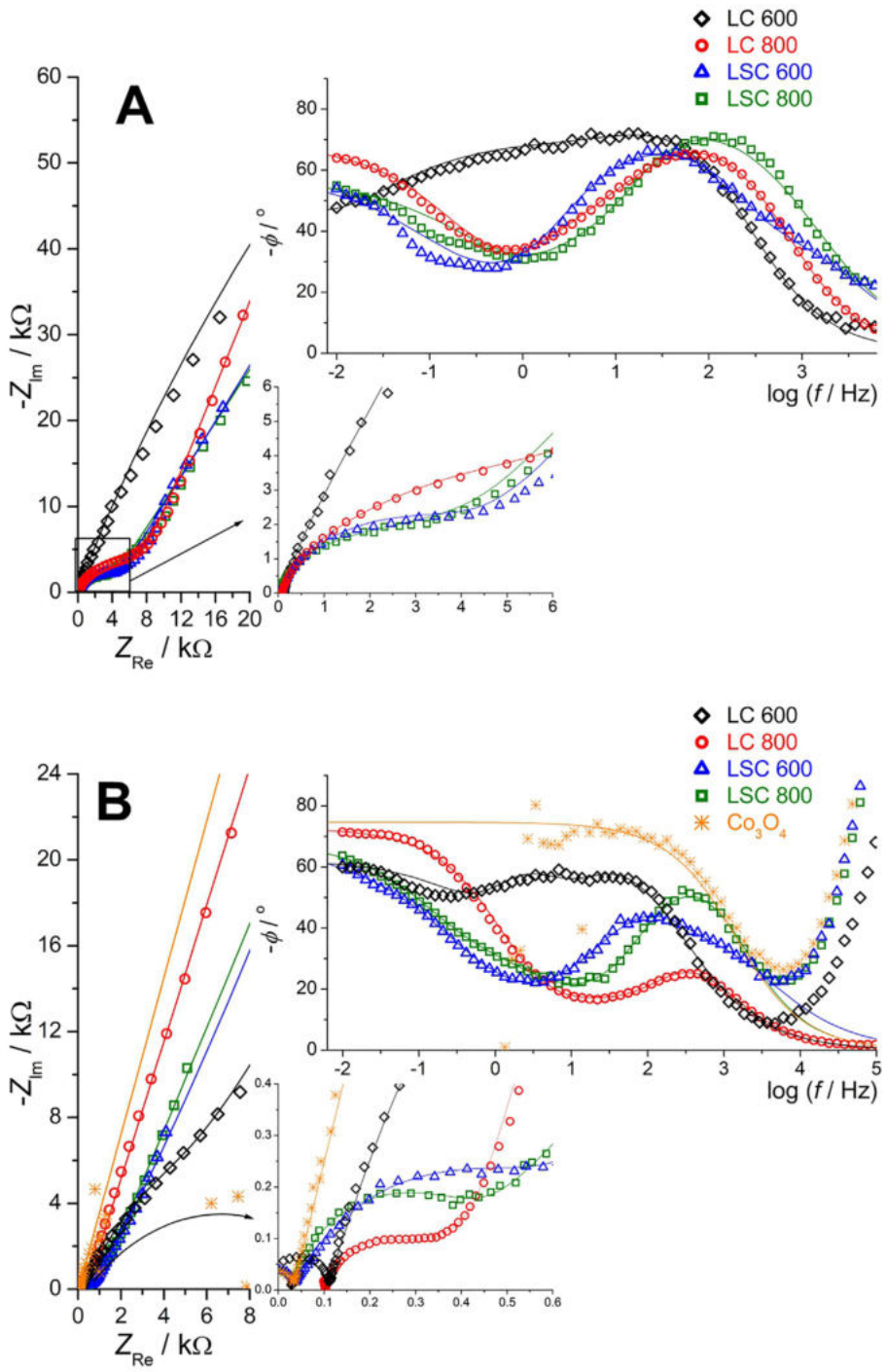

Fig. 5. Complex plane and phase shift (ϕ) plots of LC 600, LC 800, LSC 600 and LSC 800 powders, with insets showing enlarged high frequency region PEIS analysis at a) 100 and b) 300 mV.

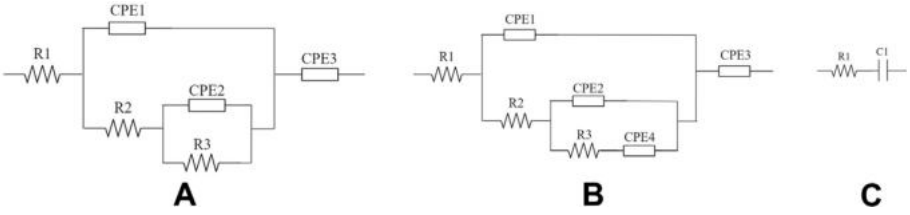

Fig. 6. The equivalent electrical circuits used to fit the impedance spectra of: a) LC 600, LC 800 and LSC 800 recorded at 100 mV and 300 mV and LSC 600 recorded at 100 mV, b) LSC 600 recorded at 300 mV and c) Co_3O_4 recorded at 300 mV.

Table 2
Electrochemical impedance spectroscopy data for LC 600, LC 800, LSC 600 and LSC 800 samples gained at 100 mV.

Sample	R1(Ω)	R2(Ω)	*R3*(Ω)	C1(μF)	*C2*(μF)	C3(μF)	C_{tot}($\times 10^2$F g^{-1})
LC 600	114	3323	2.5×10^5	9.0	4.1	136	12
LC 800	85	3300	3181	3.7	15	84	15.3
LSC 600	30	92	3701	4.0	5.0	223	8.6
LSC 800	30	1957	1351	6.4	39.4	89	30.2

Comparing the results from Tables 2 and 3 it could be noticed that the resistance that precedes the capacitive response of the material is larger by up to one order of magnitude for the measurements performed at 100 mV. The modest capacitive response of the material could be seen when compared to the response at 300 mV. The values of the calculated total capacitance, C_{tot}, are considerably lower than the values obtained by CV. This indicates that material needs a much wider perturbing measuring potential range than 10 mV (PEIS) in order to develop a full capacitive response (700 mV in CV). This is best seen in the PEIS results and EEC of the LSC 600 sample recorded at 300 mV (Table 3) where there is the considerably highest capacitance value of C3 being 12,963 μF. However, it is in series with the rest of the EEC, which gives the total capacitance of 589 $\times$ 10^{-2}F g^{-1}. This series capacitance is also characteristic for all other samples, and has the highest value in EEC. This apparently indicates that full development of the capacitive response requires some preceding reactions to occur. Since CV gives higher values, these preceding reactions could take place out of the potential range spent in PEIS perturbation. Hence, in order for full capacitive response to be evidenced, there is need for consecutive electrochemical transformations to occur.

As it was indicated by CV measurements, PEIS measurements proved that strontium promotes the structure and pseudocapacitive behavior of the synthesized perovskite material. The former statement is in good agreement with the findings that porous metal oxide structure with high specific surface area is responsible for the high C_{sp} values since it enables and promotes the Faradaic reactions. Sr promotes the capacitive response of LC and it favors and enhances redox transitions of the material in higher oxidation states.

The charging-discharging stability and rate capability towards potential applicability of the LC and LSC powders as supercapacitor electrode materials was further tested and examined by galvanostatic charge–discharge (GCD) tests. The GCD measurements were performed in 0.10 M KOH at currents of 50 and 200 μA. The results of GCD measurements of LC 600, LC 800, LSC 600 and LSC 800 powders are shown in Fig. 7.

As was discussed and explained in relation to Fig. 4, typical pseudocapacitive behavior is reflected in some deviation of the curves from full linearity [24,38]. GCD curves lack mirror symmetry in the investigated potential range due to redox reactions that occur on the electrode surface [39]. The deviation appears not dependent on the GCD rate, which indicates that related redox transitions are uniformly distributed throughout the material. At a glance, Fig. 7A–C shows the higher stability at higher curents, due to indicated distribution of the components and phases as discussed in relation to Table 1 and Fig. 3. Specific capacitances for the first and 500th cycle, gained as the mean by graphical differentiation of G-C/DCGCD curves (since a rather nonlinear response was registered (Fig. 7) [40]), according to Eq. (2). All of the calculated values for the specific capacitance obtain from GCD curves follow the order found by CV (Fig. 4) and PEIS measurements (Table 3).

The LC 600, LC 800 and LSC 600 GCD curves are almost identical in shape, representing a bell-like shape variation of the potential with time, which is a typical supercapacitor behavior, while the charge curve for LSC 800 has a half-cycle shape if compared to a more linear discharge curve as the corresponding counterpart, Fig. 7A-C. These findings are in accordance with previous research [6]. The difference between the investigated samples is that the LC 600, LC 800 and LSC 800 samples have an almost similar discharge time, while LSC 600 discharge time is almost twice of that for high-temperature samples. Although LSC 800 is of highest stability in charge/discharge cycles, it is of poor capacitive ability at the level of the LC samples.

Although the CD stability of the synthesized samples are more (high rates) or less (low rates) similar, the rate capabilities are quite different, Fig. 7D and E. It could be noted that the shape of the CD curves does not change much with the CD rate. However, the decrease in CD abilities upon increasing in CD rate was registered for all samples. The full-cycle charge exchanged at low (LR) and high (HR) CD rates, as well as that separated to half-cycles at low (LC) and high (HC) charging rates are presented in Table 4. The relative decrease of the charge exchanged with respect to low CD rates are given as corresponding δ values.

The LC 600 sample, being of lowest capacitance, also shows the lowest sensitivity to the CD rate. The decrease in charge exchanged is around 24 %, with the charging rate suffering more (27 %) than the discharging values (21%). This indicates that the interior of densely packed material (Fig. 2A) are hardly accessible at high CD rates. Once charged, however, the outer layers are relatively available more for discharge in comparison to the other samples.

Considerable larger decreases of CD rate capability are found for the other samples, with the highest one being for LSC 600 sample during charging. The mutual characteristic of LC 800, LSC 600 and LSC 800 is the initiation of (LC 800) towards the full generation of spherical structures (LSC samples), Fig. 1. Apparently, the CD dynamics “penetrate” harder into the dense internal structure of the sphere (Fig. 3). The highest decrease during the charging cycle is found for the sample of stuck spheres with a smooth surface (Fig. 1C). Consequently, LSC 600 sample suffers the most from charging rate capability decrease (59 %), but also shows the largest difference between the δ_{HC} and δ_{HD} values. This consideration is in accordance with that explained in relation to rate capability of the LC 600 sample.

Considering all previous investigations of the microstructure (SEM, EDS and XRD) to the electrochemical performances (CV, EIS and GCD) LSC 600 shows superior characteristics with respect to LC and its low temperature twin. All of these findings show the promoting influence of strontium on the supercapacitive properties, as well as the influence of the processing temperature that plays an important role in the pro-

Table 3
Electrochemical impedance spectroscopy data for LC 600, LC 800, LSC 600 and LSC 800 samples gained at 300 mV.

Sample	R1(Ω)	R2(Ω)	*R3*(Ω)	C1(μF)	*C2*(μF)	C3(μF)	C4(μF)	C_{tot}($\times 10^2$F g^{-1})
LC 600	101	710	2142	1.9	29	51	–	20
LC 800	102	231	64	3.3	133	292	–	93
LSC 600	28	240	438	2.5	3.3	12,963	611	589
LSC 800	33	412	422	3.4	347	587	–	219

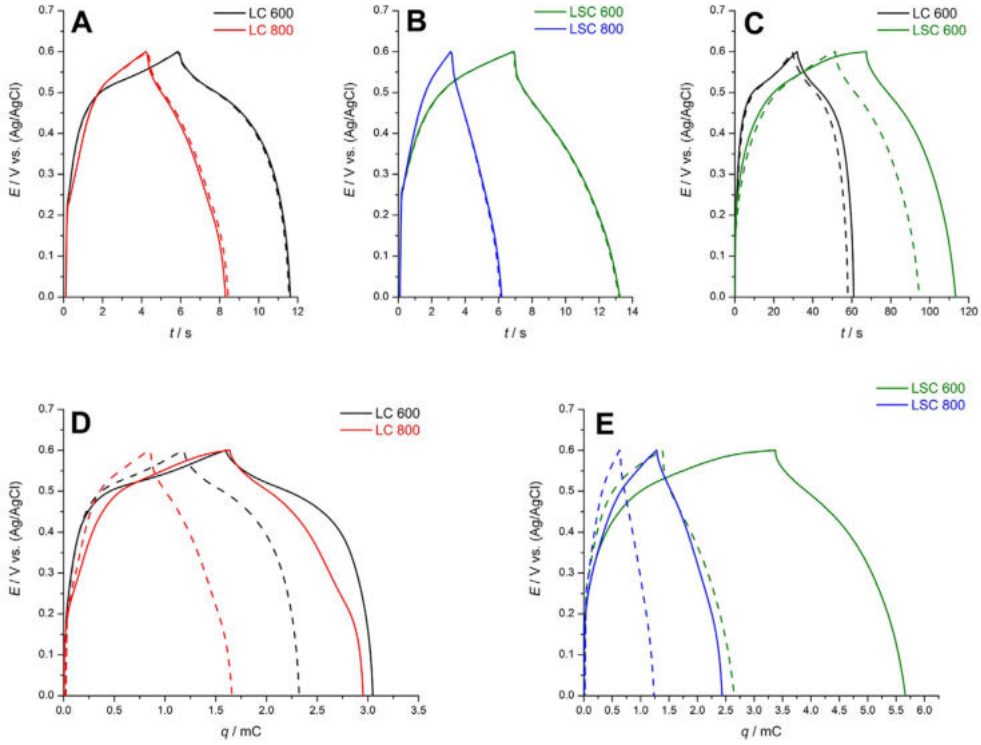

Fig. 7. Initial (full lines) and 500th (dashed lines) galvanostatic charge–discharge (GCD) curves of A) LC and B) LSC samples at the current of 200 μA in; C) the same curves for LC 600 and LSC 600 at the current of 50 μA. Rate capability tests at low (50 μA, full lines) and high (200 μA, dashed lines) of D) LC and E) LSC samples; 0.1 M KOH at room temperature.

Table 4
Charges exchanged and relative decreases of exchanged charges with respect to low CD rate at low and high CD rates for full and half cycles.

Sample	q_{LR} / mC	q_{HR} / mC	δ_{HR} / %	q_{LC} / mC	q_{HC} / mC	δ_{HC} / %	q_{LD} / mC	q_{HD} / mC	δ_{HD} / %
LC 600	3.05	2.32	23.93	1.6	1.17	26.88	1.45	1.15	20.69
LC 800	2.95	1.66	43.73	1.64	0.84	48.78	1.31	0.82	37.40
LSC 600	5.66	2.65	53.18	3.37	1.38	59.05	2.29	1.27	44.54
LSC 800	2.44	1.24	49.18	1.28	0.62	51.56	1.16	0.62	46.55

duction of electrode material. It could be concluded that LSC 600 is promising supercapacitor electroactive material with fine reversible charge–discharge performances.

5. Conclusions

The influence of strontium oxide doping into LC shows that the synthesis temperature plays an important role in the characteristics of the final material, with particles becoming more spherical and less aggregated with increasing temperature. The addition of strontium oxide further defines the formation of more spherical powders (LSC). EDS and XRD analyses of the powders suggest that that besides LC and LSC perovskite powders, some other Co-based oxides are formed.

The voltammograms show that the materials are strongly governed by Faradaic processes. Incorporation of Sr into the LC lattice leads to a considerable increase in the currents at positive potentials. The specific capacitances of the LSC samples are higher (2–4-fold) compared to the LC samples, with LSC 600 having the highest C_{sp} value.

Calculated PEIS capacitance values are lower than CV obtained values because the material needs a much wider CD potential range in order to develop full capacitive performance. PEIS shows that strontium promotes the structure and pseudocapacitive behavior of the synthesized material, favoring and enhancing the redox transition of materials in higher oxidation states.

Specific capacitance results of GCD measurements are in accordance and comparable with the values obtained from CV and PEIS measurements. The LC samples showed the lowest sensitivity to the CD rate, with the charging values suffering more than the discharging values, indicating that interior of densely packed materials are hardly accessible at high CD rates. Once charged, the outer layers are relatively more available for discharge in comparison to other samples. LSC 600 sample suffers the most from charging rate capability decrease, but also shows the largest difference between charging and discharging rates.

However, it is important to know that PEIS measurements indicated that full potential window cycling within electrolyte stability is required to gain full interactive capacitive performances of the obtained oxides as supports for supercapacitor materials.

CRediT authorship contribution statement

Miroslav M. Pavlović: Investigation, Methodology, Visualization, Writing - review & editing, Writing - original draft. **Marijana R. Pantović Pavlović:** Formal analysis, Validation, Writing - original draft. **Sanja G. Eraković Pantović:** Data curation. **Jasmina S. Stevanović:** Conceptualization. **Srećko R. Stopić:** Conceptualization. **Bernd Friedrich:** Funding acquisition. **Vladimir V. Panić:** Supervision, Writing - review & editing, Methodology.

Declaration of Competing Interest

The authors declare that they have no known competing financial interests or personal relationships that could have appeared to influence the work reported in this paper.

Acknowledgements

This work was supported by the Ministry of Education, Science and Technological Development of the Republic of Serbia (Grant No. 451-03-9/2021-14/200026). The authors would like to thank the Ministry of Education, Science and Technological Development of the Republic of Serbia and DAAD, Germany, for funding of the Project No.: 57334757.

References

[1] J. Deng, L. Kang, G. Bai, Y. Li, P. Li, X. Liu, Y. Yang, F. Gao, W. Liang, Solution combustion synthesis of cobalt oxides (Co3O4 and Co3O4/CoO) nanoparticles as supercapacitor electrode materials, Electrochim. Acta. 132 (2014) 127–135, https://doi.org/10.1016/j.electacta.2014.03.158.

[2] M.K. Lima-Tenório, C.S. Ferreira, Q.H. Felix Rebelo, R.F. Brambilla de Souza, R.R. Passos, E.A. Gómes Pineda, L.A. Pocrifka, Pseudocapacitance properties of Co3O4 nanoparticles synthesized using a modified sol-gel method, Mater. Res. 21 (2018) 1–7, https://doi.org/10.1590/1980-5373-MR-2017-0521.

[3] Y. Cao, B. Lin, Y. Sun, H. Yang, X. Zhang, Symmetric/Asymmetric Supercapacitor Based on the Perovskite-type Lanthanum Cobaltate Nanofibers with Sr-substitution, Electrochim. Acta. 178 (2015) 398–406, https://doi.org/10.1016/j.electacta.2015.08.033.

[4] Y. Wang, T. Zhou, K. Jiang, P. Da, Z. Peng, J. Tang, B. Kong, W.-B. Cai, Z. Yang, G. Zheng, Reduced mesoporous Co_3O_4 nanowires as efficient water oxidation electrocatalysts and supercapacitor electrodes, Adv. Energy Mater. 4 (16) (2014) 1400696, https://doi.org/10.1002/aenm.201400696.

[5] A. Subasri, K. Balakrishnan, E.R. Nagarajan, V. Devadoss, A. Subramania, Development of 2D $La(OH)_3$ /graphene nanohybrid by a facile solvothermal reduction process for high-performance supercapacitors, Electrochim. Acta. 281 (2018) 329–337, https://doi.org/10.1016/j.electacta.2018.05.142.

[6] S. Eraković, M.M. Pavlović, S. Stopić, J. Stevanović, M. Mitrić, B. Friedrich, V. Panić, Interactive promotion of supercapacitance of rare earth/CoO_3-based spray pyrolytic perovskite microspheres hosting the hydrothermal ruthenium oxide, Electrochim. Acta. 321 (2019) 134721, https://doi.org/10.1016/j.electacta.2019.134721.

[7] B. Kirubasankar, V. Murugadoss, S. Angaiah, Hydrothermal assisted in situ growth of CoSe onto graphene nanosheets as a nanohybrid positive electrode for asymmetric supercapacitors, RSC Adv. 7 (10) (2017) 5853–5862, https://doi.org/10.1039/C6RA25078E.

[8] S. Arunachalam, B. Kirubasankar, V. Murugadoss, D. Vellasamy, S. Angaiah, Facile synthesis of electrostatically anchored $Nd(OH)_3$ nanorods onto graphene nanosheets as a high capacitance electrode material for supercapacitors, New J. Chem. 42 (4) (2018) 2923–2932, https://doi.org/10.1039/C7NJ04335J.

[9] K. Balakrishnan, M. Kumar, S. Angaiah, Synthesis of Polythiophene and its Carbonaceous Nanofibers as Electrode Materials for Asymmetric Supercapacitors, Adv. Mater. Res. 938 (2014) 151–157, https://doi.org/10.4028/www.scientific.net/AMR.938.151.

[10] J.T. Mefford, W.G. Hardin, S. Dai, K.P. Johnston, K.J. Stevenson, Anion charge storage through oxygen intercalation in $LaMnO_3$ perovskite pseudocapacitor electrodes, Nat. Mater. 13 (7) (2014) 726–732, https://doi.org/10.1038/nmat4000.

[11] A.K. Tomar, A. Joshi, G. Singh, R.K. Sharma, Perovskite oxides as supercapacitive electrode: Properties, design and recent advances, Coord. Chem. Rev. 431 (2021) 213680, https://doi.org/10.1016/j.ccr.2020.213680.

[12] M. Wohlfahrt-Mehrens, J. Schenk, P.M. Wilde, E. Abdelmula, P. Axmann, J. Garche, New materials for supercapacitors, J. Power Sources. 105 (2) (2002) 182–188, https://doi.org/10.1016/S0378-7753(01)00937-5.

[13] P.M. Wilde, T.J. Guther, R. Oesten, J. Garche, Strontium ruthenate perovskite as the active material for supercapacitors, [1]Dedicated to Professor W. Vielstich on the occasion of his 75th birthday, J. Electroanal. Chem. 461 (1-2) (1999) 154–160, https://doi.org/10.1016/S0022-0728(98)00179-X.

[14] X. Zhang, Y. Zhao, C. Xu, Surfactant dependent self-organization of Co_3O_4 nanowires on Ni foam for high performance supercapacitors: From nanowire microspheres to nanowire paddy fields, Nanoscale. 6 (2014) 3638–3646, https://doi.org/10.1039/c3nr06734c.

[15] X.W. Wang, Q.Q. Zhu, X.E. Wang, H.C. Zhang, J.J. Zhang, L.F. Wang, Structural and electrochemical properties of $La0.85Sr0.15MnO_3$ powder as an electrode material for supercapacitor, J. Alloys Compd. 675 (2016) 195–200, https://doi.org/10.1016/j.jallcom.2016.03.048.

[16] A.K. Tomar, G. Singh, R.K. Sharma, Fabrication of a Mo-Doped Strontium Cobaltite Perovskite Hybrid Supercapacitor Cell with High Energy Density and Excellent Cycling Life, ChemSusChem. 11 (23) (2018) 4123–4130, https://doi.org/10.1002/cssc.v11.2310.1002/cssc.201801869.

[17] J.-S. Park, W.-H. Chung, H.-S. Kim, Y.-B. Kim, Rapid fabrication of chemical-solution-deposited $La0.6Sr0.4CoO_3-\delta$ thin films via flashlight sintering, J. Alloys Compd. 696 (2017) 102–108, https://doi.org/10.1016/j.jallcom.2016.11.074.

[18] B. Kirubasankar, V. Murugadoss, J. Lin, T. Ding, M. Dong, H.u. Liu, J. Zhang, T. Li, N. Wang, Z. Guo, S. Angaiah, In situ grown nickel selenide on graphene nanohybrid electrodes for high energy density asymmetric supercapacitors, Nanoscale. 10 (43) (2018) 20414–20425, https://doi.org/10.1039/C8NR06345A.

[19] K.-S. Hwang, H.-M. Lee, Y.-M. Lim, Preparation of epitaxially grown $LaSrCoO_3$ thin films on $SrTiO_3$(100) substrates by the dipping-pyrolysis process, J. Mater. Sci. 35 (2000) 6209–6212, https://doi.org/10.1023/A:1026781211253.

[20] K. Hwang, H. Lee, S. Min, B. Kang, Epitaxially Grown $LaSrCoO_3$ Thin Films on Various Substrates by the Sol-Gel Method, J. Sol-Gel Sci. Technol. 3 (2000) 175–180, https://doi.org/10.1023/A:1008725205747.

[21] A.K. Tomar, A. Joshi, S. Atri, G. Singh, R.K. Sharma, Zero-Dimensional Ordered $Sr2CoMoO_6-\delta$ Double Perovskite as High-Rate Anion Intercalation Pseudocapacitance, ACS Appl. Mater. Interfaces. 12 (13) (2020) 15128–15137, https://doi.org/10.1021/acsami.9b2276610.1021/acsami.9b22766.s001.

[22] K. Genji, K. Myoujin, T. Kodera, T. Ogihara, Synthesis and Electrical Properties of La Doped $SrTiO_3$ Powders by Ultrasonic Spray Pyrolysis, Key Eng. Mater. 582 (2014) 115–118, https://doi.org/10.4028/www.scientific.net/KEM.582.115.

[23] B. Zhang, C. Yu, Z. Li, Enhancing the Electrochemical Properties of $LaCoO_3$ by Sr-Doping, rGO-Compounding with Rational Design for Energy Storage Device, Nanoscale Res. Lett. 15 (1) (2020), https://doi.org/10.1186/s11671-020-03411-z.

[24] A.M. Al-Jumaily, A. Meshkinzar, On the Development of Focused Ultrasound Liquid Atomizers, Adv. Acoust. Vib. 2017 (2017) 1–10, https://doi.org/10.1155/2017/7861726.

[25] S. Stopić, B. Friedrich, Synthesis of Nanosized Metallic and Core-Shell Particles By Ultrasonic Spray Pyrolysis, Contemp. Mater. 2 (2018) 111–120, https://doi.org/10.7251/COMEN1702111S.

[26] J. Lü, Y. Zhang, Z. Lü, X. Huang, Z. Wang, X. Zhu, B.o. Wei, A preliminary study of the pseudo-capacitance features of strontium doped lanthanum manganite, RSC Adv. 5 (8) (2015) 5858–5862, https://doi.org/10.1039/C4RA13583K.

[27] P.S. Gaikar, S.T. Navale, V.V. Jadhav, P.V. Shinde, D.P. Dubal, P.R. Arjunwadkar, F.J. Stadler, M. Naushad, A.A. Ghfar, R.S. Mane, A simple wet-chemical synthesis, reaction mechanism, and charge storage application of cobalt oxide electrodes of different morphologies, Electrochim. Acta. 253 (2017) 151–162, https://doi.org/10.1016/j.electacta.2017.09.039.

[28] M.M. Pavlović, M.G. Pavlović, V. Cosović, V. Bojanić, N.D. Nikolić, R. Aleksić, Influence of electrolytic copper powder particle morphology on electrical conductivity of lignocellulose composites and formation of conductive pathways, Int. J. Electrochem. Sci. 9 (2014) 8355–8366.

[29] M.M. Pavlovic´, R.V. Pantović, Z. Janković, D. Nedeljković, N.D. Nikolić, M.G. Pavlović, J.S. Stevanović, Electric Conductivity of Electrolytic Copper Powder Filled Poly(Lactide-co-Glycolide) Composites, Int. J. Electrochem. Sci. 14 (2019) 9825–9837, https://doi.org/10.20964/2019.10.02.

[30] Z. Janković, M.M. Pavlović, M.R.P. Pavlović, M.G. Pavlović, N.D. Nikolić, J.S. Stevanović, S. Pršić, Electrical and thermal properties of poly(methylmetacrylate) composites filled with electrolytic copper powder, Int. J. Electrochem. Sci. 13 (2018) 291–300, https://doi.org/10.20964/2018.01.24.

[31] B. Kirubasankar, V. Murugadoss, S. Angaiah, Hydrothermal assisted: In situ growth of CoSe onto graphene nanosheets as a nanohybrid positive electrode for asymmetric supercapacitors, RSC Adv. 7 (10) (2017) 5853–5862, https://doi.org/10.1039/C6RA25078E.

[32] C. Zhang, L. Xie, W. Song, J. Wang, G. Sun, K. Li, Electrochemical performance of asymmetric supercapacitor based on Co_3O_4/AC materials, J. Electroanal. Chem. 706 (2013) 1–6, https://doi.org/10.1016/j.jelechem.2013.07.032.

[33] W. Li, X. Wang, Y. Hu, L. Sun, C. Gao, C. Zhang, H. Liu, M. Duan, Hydrothermal Synthesized of CoMoO(4) Microspheres as Excellent Electrode Material for Supercapacitor, Nanoscale Res. Lett. 13 (2018) 120, https://doi.org/10.1186/s11671-018-2540-3.

[34] S. Vijayakumar, S. Nagamuthu, G. Muralidharan, Porous NiO/C Nanocomposites as Electrode Material for Electrochemical Supercapacitors, ACS Sustain. Chem. Eng. 1 (9) (2013) 1110–1118, https://doi.org/10.1021/sc400152r.

[35] R. Tummala, R.K. Guduru, P.S. Mohanty, Nanostructured Co_3O_4 electrodes for supercapacitor applications from plasma spray technique, J. Power Sources. 209 (2012) 44–51, https://doi.org/10.1016/j.jpowsour.2012.02.071.

[36] M.P. Harikrishnan, A.J.C. Mary, A.C. Bose, Electrochemical performance of $ANiO_3$ (A= La, Ce) perovskite oxide material and its device performance for supercapattery application, Electrochim. Acta. 362 (2020) 137095, https://doi.org/10.1016/j.electacta.2020.137095.

[37] E. Cao, Y. Yang, T. Cui, Y. Zhang, W. Hao, L. Sun, H. Peng, X. Deng, Effect of synthesis route on electrical and ethanol sensing characteristics for $LaFeO_3-\delta$ nanoparticles by citric sol-gel method, Appl. Surf. Sci. 393 (2017) 134–143, https://doi.org/10.1016/j.apsusc.2016.10.013.

[38] I.N. Bkrey, A.A. Moniem, Flexible Laser Reduced Graphene Oxide / MnO_2 Electrode for Supercapacitor Applications, Int. J. Chem. Nucl. Metall. Mater. Eng. 8 (2014) 829–835.

[39] H. Mo, H. Nan, X. Lang, S. Liu, L. Qiao, X. Hu, H. Tian, Influence of calcium doping on performance of $LaMnO_3$ supercapacitors, Ceram. Int. 44 (8) (2018) 9733–9741, https://doi.org/10.1016/j.ceramint.2018.02.205.

[40] Y. Gogotsi, R.M. Penner, Energy Storage in Nanomaterials - Capacitive, Pseudocapacitive, or Battery-like?, ACS Nano 12 (3) (2018) 2081–2083, https://doi.org/10.1021/acsnano.8b01914.